



Continuum modelling of a just-saturated inertial column collapse: capturing fluid-particle interaction

William Webb¹ · Barbara Turnbull¹ · Chris Johnson²

Received: 26 July 2023 / Accepted: 18 December 2023
© The Author(s) 2024

Abstract

This work presents a simple two-phase flow model to analyse a series of axisymmetric granular column collapse tests conducted under elevated gravitational accelerations. These columns were prepared with a just-saturated condition, where the granular pores were filled with a Newtonian fluid up to the column's free surface. In this configuration, unlike the fully submerged case, air-water-grain contact angles may be important to flow dynamics. The interaction between a Newtonian fluid phase and a monodispersed inertial particle phase was captured by an inter-phase interaction term that considers the drag between the two phases as a function of the particle phase porosity. While this experimental setup has broad applications in understanding various industrial processes and natural phenomena, the focus of this study is on its relevance to predicting the motion of debris flows. Debris flows are challenging to model due to their temporally evolving composition, which can lead to the development of complex numerical models that become intractable. The developed numerical scheme in this study reasonably reproduces the particle-size and gravitational acceleration dependencies observed within the experimental runout and basal fluid pressure dissipation data. However, discrepancies between the model and physical experiments primarily arise from the assumption of modelling the granular phase as a continuum, which becomes less appropriate as particle size increases.

Keywords Two-phase · Depth averaged · Granular collapse · Just-saturated · Centrifuge modelling

1 Introduction

Granular-fluid flows have emerged as a prominent area of scientific inquiry, owing to their extensive prevalence in both industrial and natural contexts [1]. In this current study, our research focuses on a subset of natural granular mass movements that fall under the classification of gravity-driven landslides [2]. Notably, we direct our attention towards one specific type known as debris flows, which pose significant threats to communities and infrastructure situated in

mountainous regions worldwide [3]. Particularly in developing countries, population exposure to such hazards is on the rise [4]. Despite past scientific attention, the increasing frequency and intensity of flow triggering events, such as periods of high rainfall intensity [e.g. 5, 6], melting of glaciers and permafrost [e.g. 7, 8] and, production of wildfires [e.g. 9, 10], occurring near urban areas, make it imperative to gain a deeper understanding of the underlying mechanics governing debris flow behaviour.

Numerical modelling plays a vital role in the prediction and formulation of effective mitigation strategies for debris flows. The complex nature of debris flows, with comparatively high fluid volume fractions [11] and wide particle size distributions [12], presents challenges not present in other gravity-driven mass movements. As a result, both the fluid and solid phases, as well as their inter-phase interaction, significantly influence macro-scale flow behaviour [13]. To develop models that can approximate field-scale flow conditions, it is necessary to adopt an idealized flow rheology. This simplification enables the formulation of

✉ William Webb
evyww@nottingham.ac.uk

Barbara Turnbull
barbara.turnbull@nottingham.ac.uk

Chris Johnson
chris.johnson@manchester.ac.uk

¹ Department of Civil Engineering, University of Nottingham, Nottingham NG7 2RD, UK

² Manchester Centre for Nonlinear Dynamics, University of Manchester, Manchester M13 9PL, UK

tractable models that can yield valuable insights into debris flow dynamics.

Debris flows have most commonly been modelled as a single, homogeneous granular-fluid [e.g. 14, 15]. Another approach is to treat the fluid and granular material as separate continuum phases coupled by a phase interaction term [e.g. 13, 16, 17]. To simplify computations, depth averaged equations are commonly used to describe the conservation relations of the phases and the bulk flow. These equations were originally derived under the assumption of a homogeneous density profile [18]. However, this approach overlooks the fact that the solid volume fraction varies spatially and temporally, which contributes to the diverse range of rheological behaviours observed in mass movement events, including the development of excess pore pressures [19]. Field observations [e.g. 20, 21] and large-scale testing [e.g. 22] have well-documented this fact.

More recent models have sought to increase the complexity in which the two phases can be modelled separately. Some models [e.g. 23, 24] describe how the interactions between the granular and fluid phases alter flow dynamics. Iverson and George [24] do this through the generation and dissipation of excess pore pressures, while maintaining a heterogeneous flow profile by not allowing the two phases to separate. Kowalski and McElwaine [25] described each phase using separate mass equations but a single momentum equation. Gray and Kokelaar [26] achieved separation between two phases in a similar way but focussed on particle size segregation by considering two granular phases of differing particle size instead. Further phase separation has been achieved in other models [e.g. 27, 28] by describing each phase with its own mass and momentum equation.

While these recent models represent a significant improvement over earlier efforts, the diversity of modelling strategies discussed demonstrates that there is no consensus on the most appropriate way to efficiently model these two-phase flows, and that different approaches can inform us about different aspects of a flow. Additionally, these models only account for debris flows with uniform particle sizes. However, as stated by Iverson [13], and more recently demonstrated experimentally, many aspects of macro-scale flow behaviour, such as flow mobility [29], bed erosion [30], and the accumulation and dissipation of excess pore pressures [31], are highly dependent on the grain size distribution of the flow, particularly the amount of fine, silt, and clay material present. Consequently, current numerical methods do not allow the micro-scale effects from the inclusion of fine granular material to influence macro-scale flow behaviour.

One possible approach to incorporate micro-scale effects is to include them in the interphase interaction term so that they can impact the pore-scale. In this study, we aim to explore the potential of this method by examining the extent to which micro-scale effects can be accurately reproduced in

the macro-scale flow behaviour of a simplified experimental flow.

In particular, the unsteady collapse of a granular column has been a widely utilised test configuration in the last two decades to examine how the column's initial geometry and composition influence its dynamics [e.g. 33, 34, 35, 36, 37]. For the case of a dry granular collapse, where many controlling parameters exhibit scale-invariance, scaling relationships from laboratory-scale experiments have been linked to geophysical granular flows [3]. However, the inclusion of a fluid phase within the granular mixture introduces a stress-dependent grain-fluid interaction [38], causing the force ratios in laboratory-scale experiments to deviate from those in large-scale geophysical flows [39]. Achieving dynamic similarity in the crucial pore pressure control processes of the flow can be attained by artificially increasing the effective gravitational acceleration through centrifugation, as demonstrated by Webb et al. [32] in their study of axisymmetric fluid-saturated granular column collapses.

2 Experimental configuration

Webb et al. [32] performed experiments using the experimental setup illustrated in Fig. 1, which was attached to the arm of a geotechnical beam centrifuge. The experiments involved the rapid release of a granular-fluid mixture consisting of monodispersed spherical glass beads and a Newtonian water-glycerol mixture that was initially confined within a partially filled steel cylinder. It is worth noting that, while a polydispersed granular composition would have more accurately represented the composition of geophysical flows, the chosen simplification offers advantages in terms of analysing and comparing the experimental data. Furthermore, this simplification substantially reduces the complexity of the numerical model employed in attempts to replicate the collapse behaviour.

The mixture was just-saturated and allowed to spread on a horizontal plane under the influence of a prescribed gravitational acceleration g governed by the rotation rate of the centrifuge. The radius of the steel cylinder r_0 and the initial height of both the granular and fluid phases $h_{v,0}$, where $v = p, f$ corresponds to the particle and fluid phases, respectively, were equal and held constant (i.e. $h_{p,0} = h_{f,0} = h_0$). This resulted in a column aspect ratio $a = h_0/r_0 \approx 0.93$ while the particle size d , gravitational acceleration g , and fluid viscosity η_f were varied systematically to explore a wide parameter space. η_f was held constant for each test conducted at a given g , making the study primarily focused on the influence of d and g on collapse dynamics.

The study conducted by Webb et al. [32] recorded the entire evolution of each collapse within the measurement area using two high-speed cameras. Snapshots at different

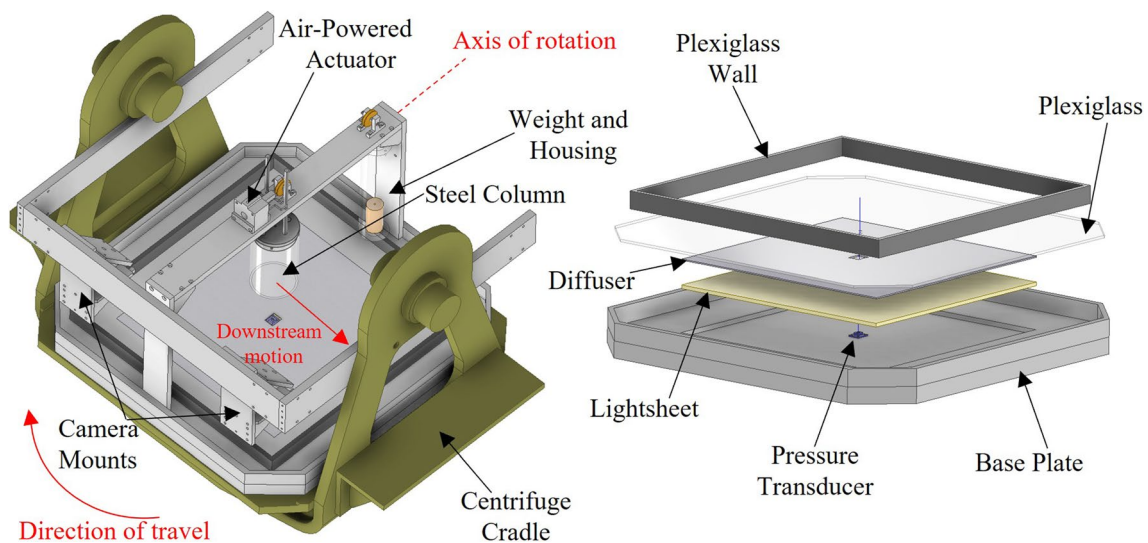


Fig. 1 The axisymmetric collapse apparatus used by Webb et al. [32]

times t from two recorded collapses are depicted in Fig. 2, where the end of the recorded collapse period is denoted as t_F (see [32] for details). A multi-threshold image analysis scheme was employed to track the average radial position of both the fluid and granular fronts throughout each collapse. Furthermore, a pressure transducer placed at the centre of the steel cylinder below the column allowed the authors to record the evolution of the basal fluid pressure at this location.

The objective of this study is to develop a numerical model that can reproduce the d - and g -dependent

behaviour observed in these granular-fluid mixture collapses. The model's accuracy will be evaluated by comparing predicted time series of runout, velocity, and basal fluid pressure with the experimental data. To simplify the analysis, all radial experimental quantities discussed will be presented as the average of upstream and downstream values. This approach is adopted due to the minimal variation observed in the collapse behaviour between the two directions, attributable to the Coriolis accelerations and the Eötvös effect commonly encountered in centrifuge modelling [40].

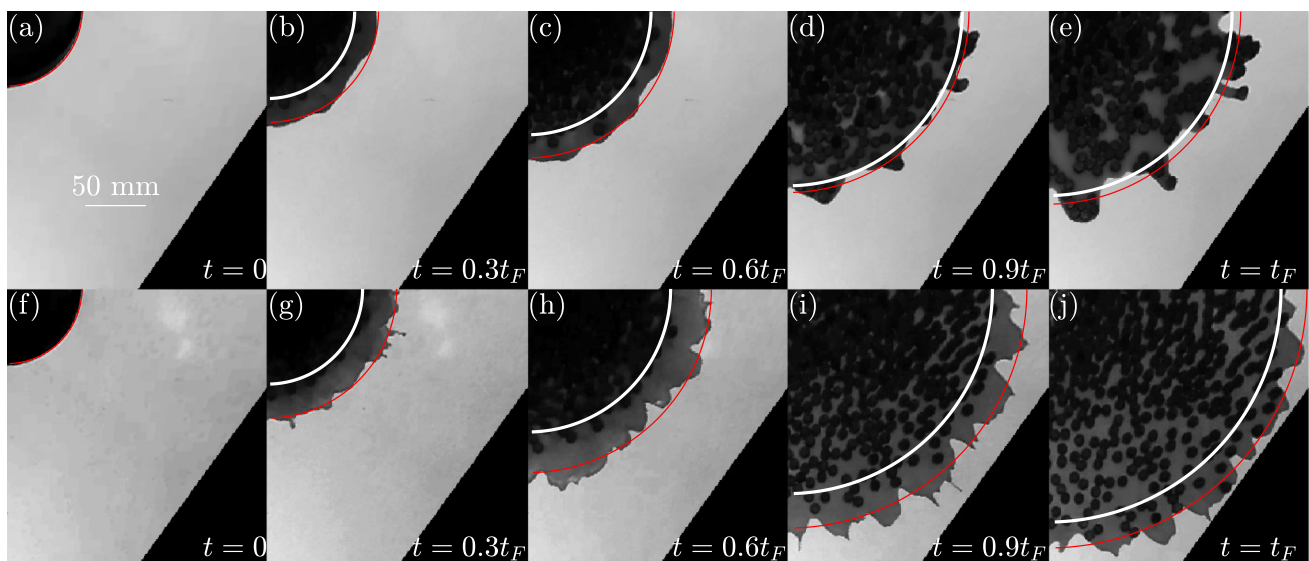


Fig. 2 Snapshots of the collapse sequence downstream of centrifuge motion for two columns, both with $d = 8$ mm, with (a)–(e) $g = 9.81$ m s⁻² and (f)–(j) $g = 137.64$ m s⁻² from Webb et al. [32]. The averaged radial position of the fluid (red) and particle (white) phase fronts are shown

3 Modelling

3.1 Depth averaged equations

A schematic representation of the numerical model used to replicate the flow dynamics observed in the experiments is illustrated in Fig. 3. The model depicts the motion of distinct granular and fluid continuum phases with specific densities ρ_v , where, again, $v = p, f$ corresponds to the particle and fluid phases, respectively, spreading across a horizontal plane. The model takes into account the separate influences of gravitational and basal drag forces on the behaviour of the two phases, while their motion is tightly coupled through a phase interaction term.

Like many previous studies on gravity-driven multiphase flows [e.g. 25, 27, 28], the current work will simplify the system of equations by depth averaging the flow to improve computational efficiency. This assumption is based on the following premises: (i) for the particle sizes considered, surface tension effects of the fluid can be disregarded [32]; (ii) the generation of excess pore pressures is eliminated through the exclusion of fine materials from the granular phase [31] and the small scale of the modelled flow [38]; and (iii) the shallow depth of the flow results in negligible accelerations perpendicular to the main direction of motion. The validity of the last assumption will be discussed in § 3.4, given the initial configuration of the granular-fluid mixture before the collapse.

Given the simplicity of the experimental flow, and in the interest of computational efficiency, it was deemed reasonable to model the motion of the flow in an axisymmetric coordinates system by only considering one lateral spatial dimension r and the vertical spatial dimension z . The nature of the experiment being modelled, and the range of particle sizes used, allows for the further assumption of an always exactly saturated or undersaturated granular phase (i.e. $h_f \leq h_p$). By employing the conversion process outlined in

Appendix A1, the original unified system of equations proposed by Meng et al. [28] is transformed into a revised set of equations. These constitute a system of depth-averaged mass and momentum conservation equations describing the evolution of the phase thickness $h_v(r, t)$ and the depth-averaged phase velocity $\bar{u}_v(r, t)$ in an undersaturated granular flow

$$\partial_t h_p + \partial_r (h_p \bar{u}_p) = -\frac{h_p \bar{u}_p}{r}, \quad (1)$$

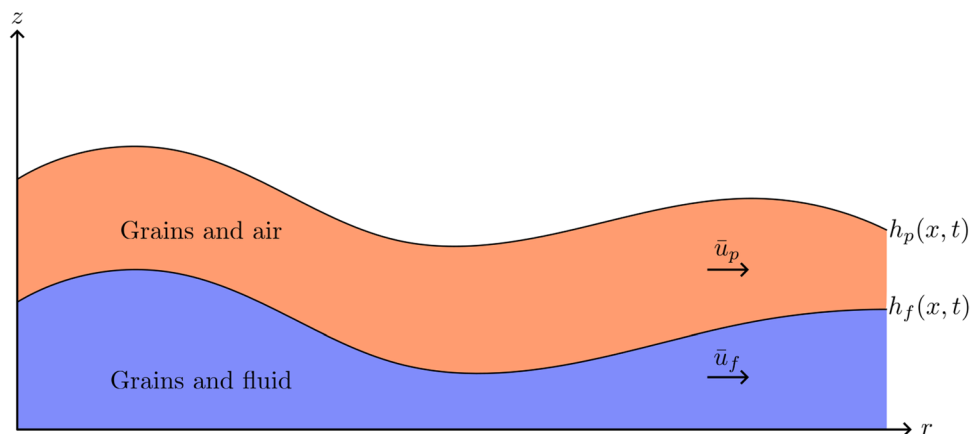
$$\partial_t h_f + \partial_r (h_f \bar{u}_f) = -\frac{h_f \bar{u}_f}{r}, \quad (2)$$

$$\begin{aligned} \partial_t (h_p \bar{u}_p) + \partial_r \left(h_p \bar{u}_p^2 + \frac{1}{2} g h_p^2 \right) \\ = -\frac{h_p \bar{u}_p^2}{r} - \mu_b \frac{\bar{u}_p}{|\bar{u}_p|} g h_p \left(1 - \gamma \frac{h_f}{h_p} \right) \\ + \frac{\eta_f \phi_f^2}{\rho_p \phi_p k} \min(h_f, h_p) (\bar{u}_f - \bar{u}_p), \end{aligned} \quad (3)$$

$$\begin{aligned} \partial_t (h_f \bar{u}_f) + \partial_r \left(h_f \bar{u}_f^2 + \frac{1}{2} g h_f^2 \right) \\ = -\frac{h_f \bar{u}_f^2}{r} + \frac{\eta_f \phi_f}{\rho_f k} \min(h_f, h_p) (\bar{u}_p - \bar{u}_f), \end{aligned} \quad (4)$$

for the particle and fluid phases, respectively, where ϕ_v is the phase volume fraction which is assumed to be constant for both phases and obey the relation $\phi_f = 1 - \phi_p$. g is the gravitational acceleration acting parallel to the z -direction, μ_b is the basal friction coefficient, γ is the density ratio between the two phases such that $\gamma = \rho_f / \rho_p$, and k is the permeability of the granular phase where $k = (\phi_f^3 d^2) / (180 \phi_p^2)$ as defined by Carman's equation [41] which has been shown to agree well with studies investigating the dynamics of sediments and bed-load transport [42, 43]. The influence of particle

Fig. 3 Sketch of a 2-D slice of an undersaturated granular collapse modelled as two coupled continuum phases



size on the dynamics is incorporated within the permeability term.

Consistent with previous studies [e.g. 27, 28], we assume that ϕ_p corresponds to a critical solid volume fraction ϕ_c , which we take to be the average solid volume fraction of the granular material before collapse. Accordingly, we set $\phi_p = \phi_c = 0.61$ and $\phi_f = (1 - \phi_c) = 0.39$. While acknowledging that the assumption of a constant ϕ_v is not valid during the later stages of the collapse (as depicted in Fig. 2), it serves as a reasonable simplification for the initial acceleration phase when the column is predominantly undergoing free-fall. To further improve computational efficiency, we approximate the $\bar{u}_p/|\bar{u}_p|$ term in equation 3 with $\tanh(\bar{u}_p/u^*)$, where $u^* = 10^{-3} \text{ m s}^{-1}$ is a velocity scale below which the granular friction is approximated as viscous. Finally, we set μ_b to 0.8 where we discuss the rationale for this value in § 3.4.

3.2 Behaviour of the model in limiting cases

The model can be reduced to the familiar case of a singular granular phase by taking $h_f = 0$. On the other hand, if the limit $h_p = 0$ is applied, we obtain a similar solution describing the motion of a singular fluid phase. However, since $\phi_f = 1 - \phi_p$ and ϕ_p is a constant, the volume of fluid per unit azimuthal angle predicted by the model would be inexact. Hence, for flow cases where both phases are present, regions of the flow that are comprised of only the fluid phase will be volumetrically incorrect. We can avoid this issue for the case of a purely fluid column collapse by setting $\phi_f = 1$ as in § 3.4.

In the case of a two-phase system, given that the interaction force between the phases remains finite, as $k \rightarrow 0$, $\bar{u}_p \rightarrow \bar{u}_f$ for all t . This implies that for the initial configuration of the physical experiments conducted by Webb et al. [32], which corresponds to a granular material that is just saturated, it is possible to say that $h_p = h_f = h(r, t)$. Therefore, by multiplying the mass and momentum continuity equations of each phase by their respective densities, ρ_v , and then summing the results, the model reduces to the equations of motion for a single phase.

Another interesting limiting case is when we consider the drainage of the fluid phase out of a low permeability static granular phase by setting $\bar{u}_p = 0$ and assuming k is small. The resulting model describes the motion of a slow fluid whose momentum depends only on the fluid pressure gradient and the phase interaction force. This system can be written as follows

$$\partial_t(h_f) + \partial_r(h_f \bar{u}_f) = 0, \tag{5}$$

$$\partial_r\left(\frac{1}{2}gh_f^2\right) = \frac{\eta_f \phi_f}{\rho_f k} h_f (-\bar{u}_f). \tag{6}$$

Rearranging equation 6 for \bar{u}_f and substituting the result into equation 5, we reassuringly recover the vector form of the Dupuit-Boussinesq aquifer flow relation [e.g. 44]

$$\phi_f \partial_t(h_f) = \frac{1}{2}g \frac{\rho_f k}{\eta_f} \nabla^2(h_f^2) = \frac{K}{2} \nabla^2(h_f^2), \tag{7}$$

where $K = (g\rho_f k)/\eta_f$ is the hydraulic conductivity of the granular phase.

3.3 Numerical method

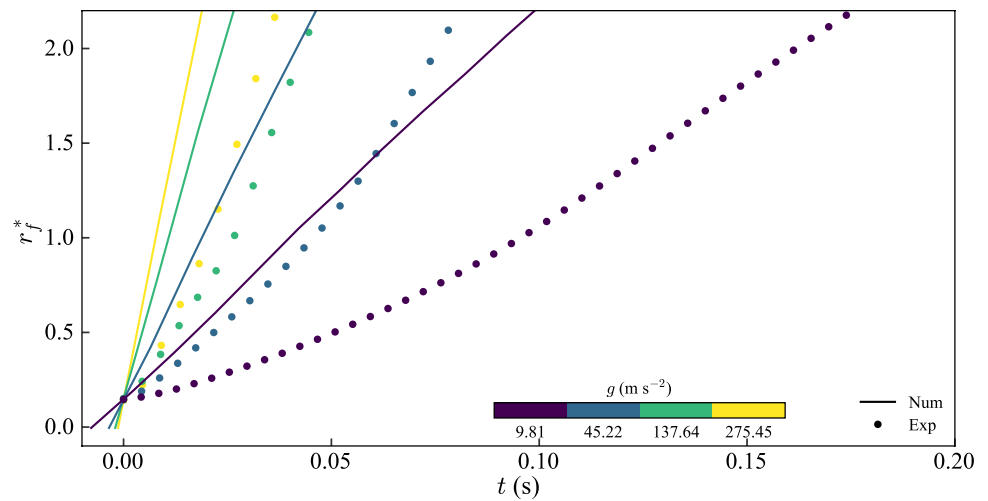
The spatial discretization of equations 1–4 was carried out using the second-order central-upwind scheme developed by Kurganov and Petrova [45] for solving the Saint-Venant system of equations. A 0.5 m test domain was discretised into 1000 cells, resulting in a cell width $\Delta r = 5 \times 10^{-4} \text{ m}$. Given that the column expands into regions where no grains are initially present, it was important to ensure that the model was positivity preserving, i.e., capable of handling the transition between cases where $h_v \neq 0$ and $h_v = 0$ [27]. To achieve this, the more sophisticated cell boundary depth correction algorithm of Chertock et al. [46] was employed. An explicit second-order Runge–Kutta method was implemented to discretise the system in time. To ensure the stability of the scheme, a CFL number of 0.2 was used. The system’s phase data was stored at time intervals $\Delta t = 1 \times 10^{-3} \text{ s}$.

3.4 Regularisation of vertical velocity components

To begin to assess the validity of the model, we start by conducting a comparison with the experimental findings for a single fluid phase only collapse (i.e. $\phi_f = 1$ and $\phi_p = 0$). For the numerical model, we define the instantaneous phase front position $r_v(t)$ as the largest radial distance where $h_v(r, t) > 0.1 \text{ mm}$ while the definition for the experimental case remains the same as in Webb et al. [32]. Similarly, we introduce the normalised phase runout length r_v^* , defined as the normalised difference between the instantaneous position of the phase front and the initial column radius $(r_v - r_0)/r_0$.

A comparison of the numerical and experimental temporal evolution of r_f^* for purely fluid columns across all tested values of g is visualised in Fig. 4. In the experimental case, the visibility of the collapsing column is initially obstructed by the steel cylinder used to construct it, causing a delay between the release of the column and the captured motion of the phase fronts in the camera footage. To address this issue, the numerical evolution of r_f^* has been shifted to align with the experimental signal by setting the r_f^* at $t = 0$ for the numerical signal to the r_f^* for the experimental signal at $t = 0$ for each respective collapse test. This alignment approach was compared against the manual determination of the

Fig. 4 Comparison of the numerical and experimental temporal evolution of the normalised average fluid runout length r_f^* with time t for purely fluid column collapses for all values of g



cylinder’s release time by analysing the collapse images. The comparison indicated that both methods yielded similar results in terms of the magnitude of the temporal offset. However, unlike the fitting approach, manually identifying the release time of the column was prone to human error, which could introduce significant variations in the magnitude of the temporal offset. This was more of an issue for the the higher g tests where the duration of the collapses are relatively short compared to the frequency of image capture, which remained constant and, therefore, independent of the applied gravitational force.

It is evident from Fig. 4 that the velocity of the fluid phase front in the numerical model is significantly higher than that observed in the corresponding experimental data at all values of g . This is to be expected since the initial configuration of the fluid columns does not meet the shallow depth assumption crucial to the model’s derivation, namely $a \ll 1$ does not hold, and equations 3 and 4 do not incorporate terms accounting for the vertical acceleration of the two phases or their subsequent dissipation upon impact with the horizontal plane [47]. We note that, if a Chézy style basal drag term were added for the fluid phase, it would decelerate the simulated fluid phase front, whereas the experimental fluid fronts accelerate over the spreading distances considered.

In order to address this issue, we implemented the mass ‘raining’ scheme as described in Larrieu et al. [47]. Originally designed for a singular granular phase, the scheme divides the flow into two distinct components. The first component consists of a shallow layer of material that spreads horizontally, with a height smaller than that of the experimental column being simulated. The second component, known as the ‘rain’, is gradually introduced to the flow over a

specific duration equivalent to the free-fall of the column. By incrementally adding mass, the injected potential energy into the modelled system is significantly reduced compared to the potential energy of the complete column. Consequently, the effects of energy dissipation during the collapse can be mimicked in the model.

In our study, we extend the application of this scheme to both the granular and fluid phases. The adjusted initial configuration of each phase, denoted as $v = p, f$, can be characterised by its initial radius r_0 , and initial height $h_{v,1} = C_r r_0$. Thus, the progressive supply of mass to the flowing material in each phase is quantified using a phase-specific volume flux per unit area

$$q_v(r, t) = \begin{cases} gt & \text{for } 0 \leq r \leq r_0 \\ 0 & \text{for } r > r_0, \end{cases} \tag{8}$$

up to a time related to the free-fall of the specific column phase $t_{v,ff} = \sqrt{2(h_{v,0} - h_{v,1})/g}$. Accordingly, the mass conservation equations 1 and 2 become

$$\partial_t h_p + \partial_r (h_p \bar{u}_p) = -\frac{h_p \bar{u}_p}{r} + q_p, \tag{9}$$

$$\partial_t h_f + \partial_r (h_f \bar{u}_f) = -\frac{h_f \bar{u}_f}{r} + q_f. \tag{10}$$

for the fluid and particle phases, respectively. Following Larrieu et al. [47], no source term was added to the momentum equations, as it is assumed that the mass is added with no horizontal momentum (i.e. in a state of free-fall).

A comparison between the temporal evolution of r_f^* for purely fluid columns at all tested values of g for both

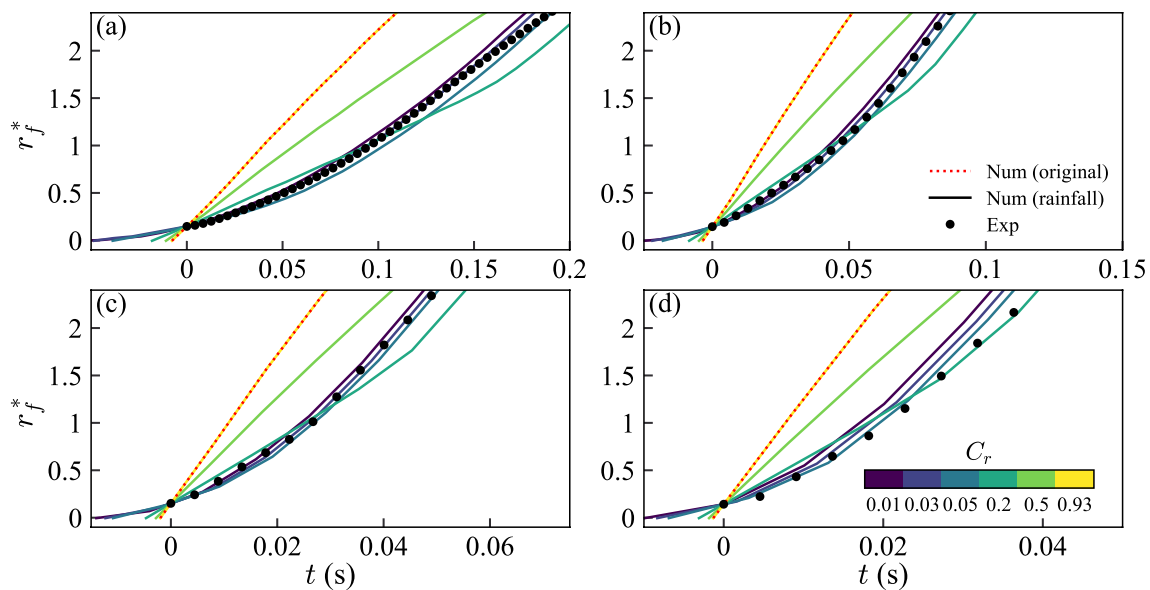


Fig. 5 Comparison of the two numerical schemes, the original and the one now utilising the mass introduction scheme of Larrieu et al. [47], and experimental temporal evolution of the normalised average fluid runout length r_f^* with time t for purely fluid column collapses

numerical models and the experimental data is shown in Fig. 5. For the numerical model utilising Larrieu et al.'s mass rainfall scheme (i.e. mass conservation equations 9 and 10), the value of C_r has been varied.

As in Fig. 4, the numerical evolution of r_f^* has been offset from the experimental signal to ensure that r_f^* at $t = 0$ for both signals is equal for each respective collapse test. Firstly, The temporal evolution of r_f^* by the numerical model employing the mass rainfall scheme matches the results of the original scheme when $C_r = 0.93$ (see Fig. 5). This is because, when $C_r = a$, $h_{v,0} = h_{v,1}$ resulting in no mass being added to the initial system as $t_{v,ff} = 0$. It is also shown that adjusting the phase mass conservation equations significantly improves the agreement between the model and experiments regardless of the value of C_r .

To ensure consistency, a C_r value of 0.05 is used from this point on as it provides the best compromise for simulating tests at all g levels. Larrieu et al. [47] found that using $C_r \leq a$ had no effect on the long-term spreading dynamics of the collapse. Therefore, the range of C_r values considered here only affects short-term spreading dynamics.

Finally, we adopt the assumption that $\mu_b = 0.8$ based on the coefficient determined Larrieu et al. [47] who used it to reproduce the runout scaling laws proposed in previous works [33, 48] for a dry axisymmetric granular column collapse (where $\phi_f = 0$ and $\phi_p = 1$). This coefficient is notably high and may

with varying values of C_r for (a) $g = 9.81 \text{ m s}^{-2}$, (b) $g = 45.22 \text{ m s}^{-2}$, (c) $g = 137.64 \text{ m s}^{-2}$ and (d) $g = 275.45 \text{ m s}^{-2}$

be attributed to the lack of consideration of interior flow dissipation mechanisms in shallow water models.

4 Calibration assessment

4.1 Runout

After tuning the model parameters using purely fluid collapse test data, we proceed to evaluate the model's ability to describe the collapse of granular-fluid mixtures by comparing the temporal evolution of r_f^* and r_p^* with experimental results for all values of d and g .

By considering the pre-collapsed column configuration, we can characterise the modeled system using both dimensionless parameters, γ and a , and three dimensional parameters, g , h_0 and $\eta_f/(\rho d^2)$, where ρ represents the effective column density $\rho = \phi_p \rho_p + \phi_f \rho_f$ [32]. These dimensional parameters can be combined to yield another dimensionless group, denoted as $B = (gd^4 \rho^2)/(h_0 \eta_f^2)$, which is analogous to the square of the ratio of the column Bond Bo and Capillary Ca numbers $(\text{Bo}/\text{Ca})^2$. Webb et al. [32] found Bo/Ca to be a key parameter in the prediction of the maximum phase front velocity.

Considering that a remains constant and γ exhibits only minor variations of approximately 8 % across the

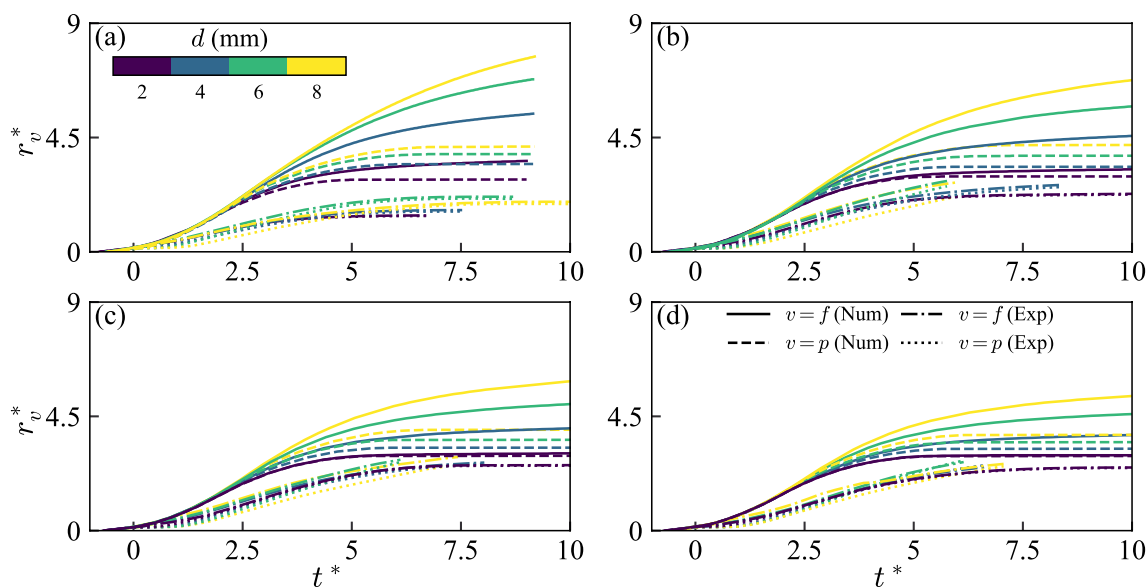


Fig. 6 Comparison of the numerical and experimental temporal evolution of the normalised phase runout length r_v^* with normalised time t^* for collapses containing a particle phase at (a) $g = 9.81 \text{ m s}^{-2}$, (b) $g = 45.22 \text{ m s}^{-2}$, (c) $g = 137.64 \text{ m s}^{-2}$ and (d) $g = 275.45 \text{ m s}^{-2}$

parameter space under investigation, we plot the runout evolution of the numerical simulations in dimensionless $r_v^* - t^*$ space. Here, t^* represents the ratio between t and the characteristic column inertial timescale $\sqrt{h_0/g}$. This approach yields a family of curves primarily determined by the value of B (Fig. 6). Specifically, when $B \ll 1$, it corresponds to tightly coupled grains and fluid, wherein the collapse is governed by drag forces. On the other hand, when $B \gg 1$ it indicates nearly independent behaviour between the grains and fluid phases.

To ensure consistency, we have, again, offset the numerical time signal from the experimental time signal. Both the fluid and particle phases have been offset by the same time period, such that their r_f^* values are equal at $t^* = 0$. This strategy enables the numerical fluid and particle runout time series to remain in phase.

The overall evolution of a collapsing mixture, previously reported by Webb et al. [32] and many other authors [e.g. 49, 50], is successfully replicated in the model (Fig. 6). The collapse consists of acceleration, quasi-steady, and retardation stages, with the duration of each stage primarily controlled by g , with each stage duration decreasing as g increases. The simulations also partially reproduce the particle-size-dependent (i.e., pore space dependent) behaviour observed in the experiments. Specifically, the model incorporates a permeability-dependent interaction term in equations 3 and 4 to exhibit the effects of granular capillarity, resulting in the fluid phase front of a collapse containing a coarser particle phase (i.e., larger

d) achieving higher peak velocities and separating itself further from the particle phase front [32].

The runout distances predicted by the model for both phases overestimate those measured experimentally for every test case. However, it is evident that, for a given g , the performance of the model improves as d decreases. Given that the volume of the granular phase is constant across all of the experiments, this is likely due to the collapses with a granular phase consisting of smaller particles, containing more particles. Hence, it is more appropriate to model the granular phase as a continuum. Moreover, the model's prediction of the final runout and the temporal evolution of the particle phase improves as g increases. This is because capillary interaction between particles becomes less significant as the particle inertia increases with g [38]. We do not model capillary interactions, hence model and experiment become more closely matched at higher g .

The omission of capillary forces likely contributes to the significant overestimation of the separation between the phase fronts during the collapse. To address this effect, it would be worthwhile to explore the incorporation of the Capillary number Ca into the phase interaction term, as a means to consider the influence of grain-scale surface tension effects [32]. However, investigating this aspect is beyond the scope of the present study.

Additionally, the assumption of a constant fluid velocity profile with flow depth (i.e., plug flow), and the omission of a fluid drag term, does not consider the increased viscous stress imposed on the fluid by the horizontal plane as the fluid depth reduces, resulting in a more turbulent flow [51], which is the case during a significant portion of the collapse

spreading stage. Nevertheless, the reduction in the separation between the two phases as g increases is encouraging, suggesting that particle inertial (i.e. d) effects become less dominant with increased scale, given that the macro-scale dynamics of geophysical-scale debris flow behaviour are primarily driven by gravitational and viscous forces [13].

4.2 Velocity

In this section, we compare the temporal evolution of the phase front velocity u_v for both the experimental and numerical test cases. The normalised phase front velocity $u_v^* = u_v / \sqrt{h_{v,0}g}$ is presented against t^* for all collapses containing a particle phase and all values of g in Fig. 7 where, again, the numerical simulation for each test has been offset from the experimental data in the time domain. As discussed in § 4.1, Fig. 7 demonstrates that the experimental evolution of both phases throughout the collapses, for all values of d and g , comprises three distinct stages of motion, including a steady state. In contrast, the simulated collapse fronts never appear to reach a steady state of motion. Similar to the the temporal evolution of r_v^* , the peak velocities of the phase fronts observed in the experiments were lower than those predicted by the simulations for all test cases. Although the simulations reasonably modelled the time after collapse initiation when these peak velocities occur, they tended to be faster than those observed in the experiments. We attribute the discrepancies between the simulation and experimental results for the temporal evolution of u_v^* primarily to the

continuum modelling assumption and the resulting transfer and dissipation of granular momentum, particularly for larger particle sizes.

Analysing the collapses in $u_v^* - t^*$ space further highlights the interference of the steel column on the acceleration stage of the experimental collapses. A particle size-dependent lag, where the granular phase front begins to move, was observed for all values of g , and the magnitude of the lag increased with d . This result is due to the larger particle sizes being trapped by the rising column for longer since the speed at which the column is lifted is proportional to g . The lifting speed of the column was designed to comply with Sarlin et al.'s [52] criterion, which defines a threshold lift velocity that prevents the release mechanism from influencing the dynamics of a collapsing dry granular phase. Contrary to the suggestion of Li et al. [53], we found that this criterion cannot be lowered for a granular material in the initially just-saturated condition. Although increasing the mass of the counterweight used to lift the column could have achieved greater column lifting speeds, it would likely have an adverse effect on the release of the granular material due to the increased viscous stresses induced between the inner walls of the cylinder and the saturated granular mixture. This effect is discussed in detail in § 5.1.

Since the particle phase is initially held stationary by the rising column, the initial discharge of the fluid phase is highly dependent on the capillarity of the granular phase (i.e. d). Hence, the peak value of u_f^* during the acceleration stage

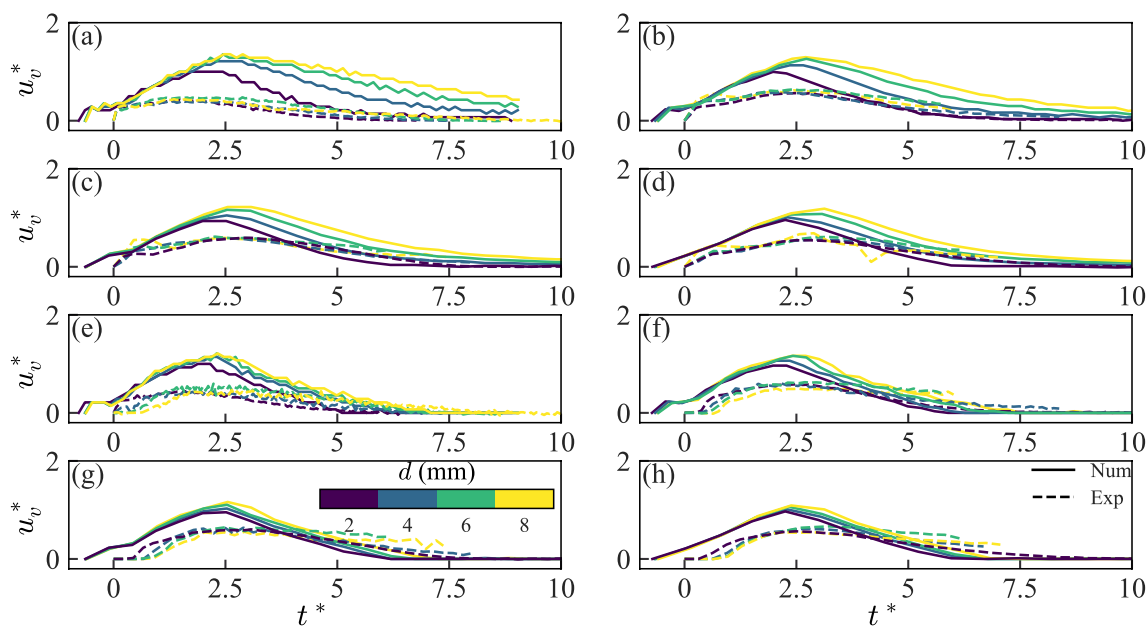


Fig. 7 Comparison of the numerical and experimental evolution of the normalised phase front velocity u_v^* with normalised time t^* where (a)–(d) $v = f$ and (e)–(h) $v = p$ for collapses containing a parti-

cle phase at $g = 9.81 \text{ m s}^{-2}$ ((a), (e)), $g = 45.22 \text{ m s}^{-2}$ ((b), (f)), $g = 137.64 \text{ m s}^{-2}$ ((c), (g)) and $g = 275.45 \text{ m s}^{-2}$ ((d), (h))

increases with d at all values of g . As found by Webb et al. [32], the dependency on d is not as prominent at $g = 9.81 \text{ m s}^{-2}$ as surface tension effects have a large influence on the initial fluid front velocity at low g . The influence of d increases as g increases to 45.22 m s^{-2} and begins to reduce for subsequent increases in g as gravitational and viscous forces begin to dominate flow dynamics.

5 Fluid pressure

With the model parameters calibrated to best match the experimental runout data, we will use these settings to predict the evolution of basal fluid pressure at the column's centre and compare it to the corresponding observations from the physical experiments.

5.1 Experimental pressure signal reduction

Upon collapse initiation, the significant acceleration of the steel cylinder relative to the initial motion of the collapsing mixture induces viscous shear stresses between the two surfaces that are capable of partially lifting the collapse material. This causes the fluid pressure being applied to the pressure sensor at the base of the column P to drop and subsequently rise when the weight of the collapsing material overcomes the viscous shear stresses impeding its downward motion. This experimental discrepancy appears to have no influence on the pressure variation observed during the initial dilation of collapsing material containing a granular phase, which was investigated previously [32], as it occurs after the pressure spike associated with the dilative motion of the collapsing mixture and over a much longer timescale. The duration of this effect is largely dependent on the column composition. For purely fluid collapses, the column's influence dissipates $t \approx \sqrt{h_0/g}$ after collapse initiation. However, for collapses containing a granular phase, the effect is prolonged, and increases with decreasing d , due to the capillary action introduced by the presence of a granular matrix.

As these complexities are not indicative of an initially unconstrained collapse, and would not be replicated within the numerical model, the pressure time series for each test was reduced to remove these effects by only considering pressure data after which the collapsing mixture had lost contact with the steel column. This also limits the contribution of the flow's vertical acceleration on the pressure measurement. As was the case in Webb et al. [32], only pressure data from the collapses undertaken at $g = 45.22 \text{ m s}^{-2}$ and $g = 137.64 \text{ m s}^{-2}$ were considered, as pressure measurements were not recorded for tests undertaken at $g = 275.45 \text{ m s}^{-2}$ and the pressure signals for tests where $g = 9.81 \text{ m s}^{-2}$ had significant signal-to-noise ratios. Unfortunately, the

sensor was damaged during the test with $d = 2 \text{ mm}$ and $g = 137.64 \text{ m s}^{-2}$, and therefore had to be removed from the dataset.

In line with the previous work, a fourth-order low-pass Butterworth filter with a cutoff frequency $f_c = 100 \text{ Hz}$ was employed to filter the pressure signal for each test. To determine the time at which the mixture no longer made contact with the steel column, multiple steps were taken. First, the pressure time series was normalised with respect to the hydrostatic pressure of the column before collapse $\mathcal{P} = \rho_f g h_{f,0}$ to obtain $P^* = P/\mathcal{P}$. Next, a surrogate signal was constructed that only included the data points corresponding to the last time when the signal was roughly equal to a constant A , where A ranged from 0.001 to 0.99 in increments of 0.001. Consequently, the surrogate signal decreased between each data point and did not increase with time. By using a lower threshold value of $A = 0.3$, the largest difference in time between consecutive points in the surrogate signal was identified as the time during which the column lifting effects were significant. As a result, the start of the reduced signal was set as the first data point after this prolonged time difference. Finally, the endpoint of the reduced signal was identified as the start of the longest concurrent subsequence during which the dimensionless pressure gradient P^*/t^* , remained below the selected threshold gradient $B = 0.1$.

The normalised reduced pressure data was fitted to a three-parameter exponential curve

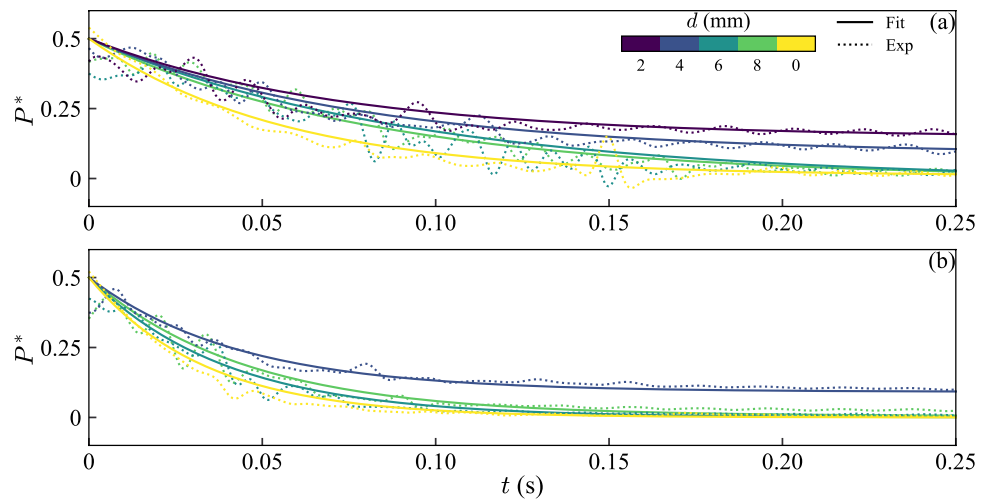
$$P^* = a \exp(-bt^*) + c, \quad (11)$$

where a , b and c are constants. This fitting procedure enables a trend to be extrapolated, which is useful for directly comparing the pressure time series of different collapse tests (see Fig. 8). As the reduced signal began at an average normalised pressure of $P_r^* = 0.45 \pm 0.03$, we consider pressure trends up to $P^* = 0.5$. Given the satisfactory representation of the experimental data by the exponential fit, we henceforth refer to the fitted trend as the experimental data.

5.2 Numerical pressure signal reduction

Since the numerical model assumes shallow-water conditions, the basal fluid pressure at the centre of the column during the simulated collapse tests is determined by the equation $P = \rho_f g h_{f|r=r_0/2}$. The utilisation of Larrieu et al.'s [47] mass 'raining' scheme results in the basal fluid pressure prior to collapse initiation $P_0 = C_r \mathcal{P}$. During the collapse tests, the injection of fluid phase mass into the system causes P to increase gradually until it reaches a value of approximately $0.8\mathcal{P}$ at $t = t_{f,ff}$ before dissipating as expected for an unconstrained collapse. To enable a direct comparison between the model predictions and experimental findings, we only analysed the basal fluid pressure data from each

Fig. 8 The raw and fitted experimental temporal evolution of the reduced dimensionless basal fluid pressure at the centre of the column P^* with time t at (a) $g = 45.22 \text{ m s}^{-2}$ and (b) $g = 137.64 \text{ m s}^{-2}$



simulation starting from the time when $P = 0.5\mathcal{P}$ for the final time.

5.3 Definition of pressure dissipation

Before comparing the numerical and experimental pressure time series, it is crucial to understand the constraints imposed by the data collection process on our analysis. Typically, the dissipation of fluid pressure is considered from a Lagrangian reference frame, where the time series records the evolution of pressure for a fixed ‘packet’ of the flow during collapse [51]. This approach allows you to analyse how internal flow deformations, such as particle suspension and no suspension within the fluid phase, promote the generation or dissipation of non-hydrostatic pore pressures [54].

However, in practical scenarios, recording pressure data from a Lagrangian reference frame is often unfeasible. Previous studies have addressed such challenges in natural flows by measuring the fluid pressure at a fixed location in the flow (Eulerian reference frame) and the height of the flow’s free surface passing over that point H [e.g. 21]. By comparing the recorded pressure with the theoretical pressures of complete granular phase suspension ($\rho g H$) and sedimentation ($\rho_f g H$), an estimation of the amount of suspended granular material within the flow can be made.

In our study, the evolution of flow height cannot be determined from the test images, which prevents the consideration of excess pore pressures at the measurement location. However, we can assess the influence of excess pore pressures within the reduced pressure signal by calculating the timescale of slope-normal diffusion of excess pore-fluid pressure $(\eta_f H^2)/(kE)$, where E is the elastic bulk modulus of the solid–fluid mixture, which is approximated as $E = 10^7 \text{ Pa}$ [38]. For our tests, the timescale values range from $10^{-5} - 10^{-3} \text{ s}$, which is at least two orders of magnitude smaller than the time at which the reduced pressure signal

begins (approximately 0.08 s and 0.05 s after collapse initiation for tests at gravitational accelerations of 45.22 m s^{-2} and 137.64 m s^{-2} , respectively). Therefore, it is reasonable to assume that all excess pore pressures have dissipated before the reduced pressure signal is captured. Consequently, the remaining fluid pressure component within the reduced signal can be assumed to be hydrostatic and dependent only on the height of fluid above the sensor location.

Based on these assumptions, and as described by the numerical model, the temporal evolution of the reduced pressure signal corresponds to the spreading of fluid away from the centre of the column. Thus, when referring to pressure dissipation, we mean the reduction in hydrostatic pressure in the Eulerian reference frame due to the spreading of the fluid phase away from the pressure sensor.

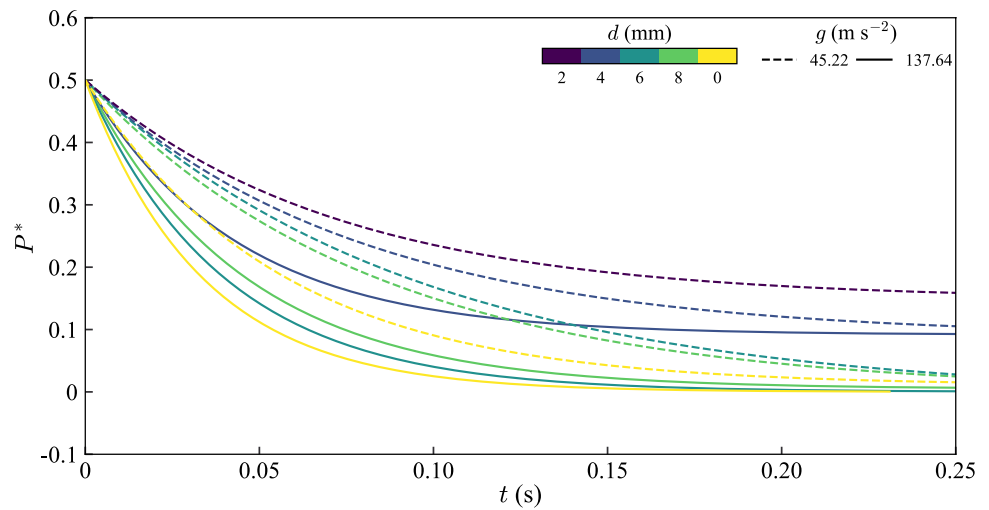
5.4 Comparison of pressure dissipation

The temporal evolution of the reduced normalized basal fluid pressure at the centre of the column P^* , obtained from the physical experiments, is shown in Fig. 9. The figure indicates that, in general, for a given g , the rate of pressure dissipation increases with increasing pore space (i.e. increasing d). Collapse tests that involve only a fluid phase, corresponding to an infinite pore space (or $d = 0 \text{ mm}$), act as an upper bound for the experiments that contain a granular phase.

The collapses involving 8 mm particles may experience a lower rate of pressure dissipation due to the column release mechanism. As shown in Fig. 7, a substantial amount of fluid drained out of the granular skeleton while it was restrained by the column. This would lead to a higher initial pressure drop, resulting in a slower rate of dissipation over the duration of the pressure signal under consideration.

In contrast, the residual value of P^* at $t = 0.25 \text{ s}$ also exhibits a dependence on d but, increases as d decreases. This trend is likely attributable to the smaller pore spaces

Fig. 9 Experimental temporal evolution of the reduced dimensionless basal fluid pressure at the centre of the column P^* with time t for varying d and g



and increased capillary forces, which make it more difficult for the fluid to escape from the granular phase, resulting in higher residual fluid pressures at the collapse centre. Conversely, for tests involving larger particle sizes (i.e. 6 and 8 mm), the residual pressure at the centre of the column approached 0, which was also the case for the pure fluid collapses.

Encouragingly, the patterns observed in the evolution of P^* with t , as depicted in Fig. 10, through the numerical model, display similar correlations with g and d . The incorporation of a d -dependent interaction term leads to an increase in the rate of pressure dissipation with increasing d , for a given g . Although the model forecasts residual pressures at $t = 0.25$ s that grow with decreasing d , they do not approach 0 for larger particle sizes. Additionally, in all scenarios, the residual pressure is overestimated by the model, likely due to the assumption of a continuous granular phase, which results in an overestimation of the magnitude of the interaction term and the selection of a

high μ_b value, which was necessary to reduce the phase front velocities.

Comparison of the numerical simulations to the experimental results by constraining g , as shown in Fig. 11, demonstrates that in all cases, similar to the temporal evolution of u_v^* , the predicted rate of pressure dissipation by the model is higher than that observed in the experiments. It is probable that this inconsistency is mainly due to the assumption of a hydrostatic pressure distribution and neglecting the vertical accelerations experienced by both constituent phases during the initial collapse of the column, which would increase the force and subsequently the pressure, applied to the horizontal plane located at the basal surface.

In order to evaluate the pressure scaling relations predicted by the model, it is essential to compare the experimental and numerical results in $P^* - t^*$ space, as illustrated in Fig. 12. As the only source of momentum transfer for the fluid phase is via its interaction with the granular phase, it is reassuring to observe that the experimental and numerical

Fig. 10 Simulated temporal evolution of the reduced dimensionless basal fluid pressure at the centre of the column P^* with time t for varying d and g

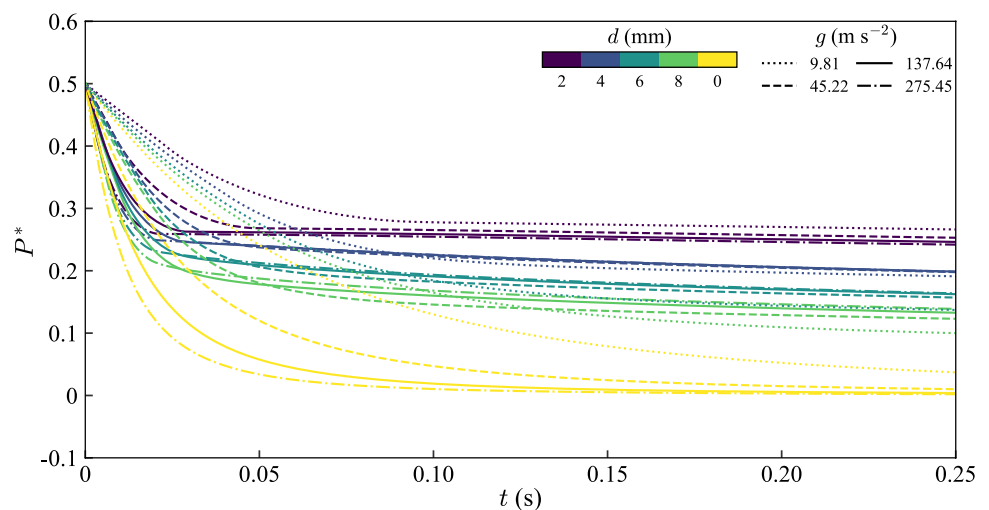


Fig. 11 Numerical and experimental temporal evolution of the reduced dimensionless basal fluid pressure at the centre of the column P^* with time t for varying d at (a) $g = 45.22 \text{ m s}^{-2}$ and (b) $g = 137.64 \text{ m s}^{-2}$

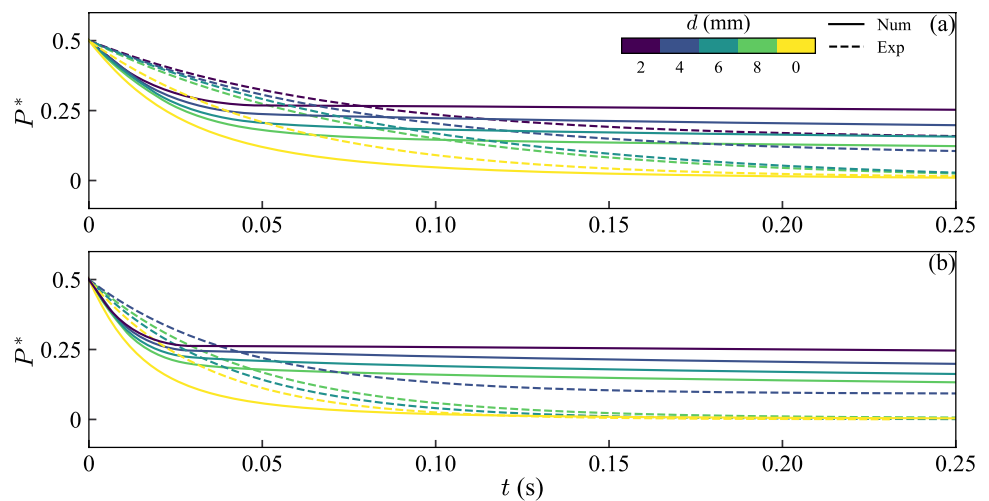
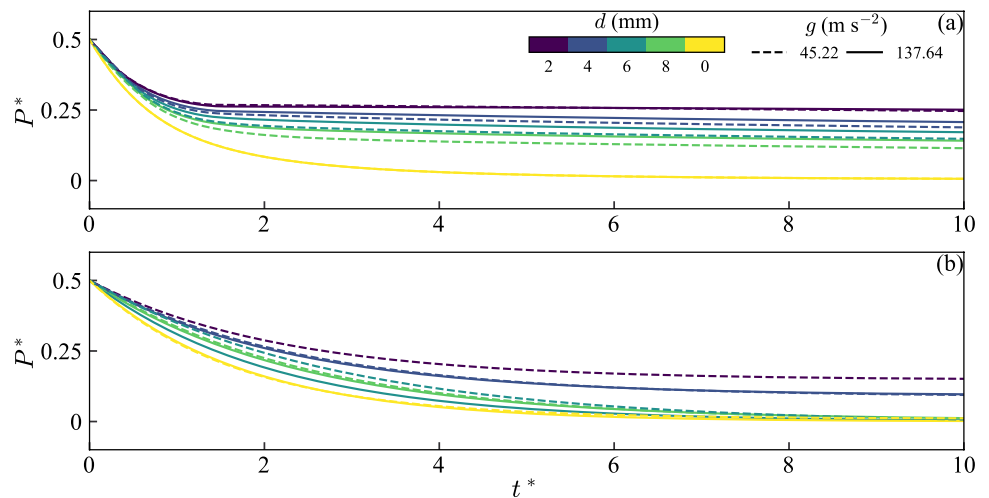


Fig. 12 (a) Numerical and (b) experimental temporal evolution of the reduced dimensionless basal fluid pressure at the centre of the column P^* with normalised time t^* for varying d and $g = 45.22 \text{ m s}^{-2}$ and 137.64 m s^{-2}



curves for the purely fluid collapses (i.e. $d = 0 \text{ mm}$) conducted at different g levels approximately collapse onto single curves, respectively. This reaffirms that, within the tested parameter range, the dissipation of basal fluid pressure during fluid column collapses is predominantly determined by the magnitude of g , while particle size effects play a secondary role.

Additionally, analysing the data in $P^* - t^*$ space demonstrates that for a specific particle size, the pressure dissipation curve's gradient for the experimental data increases with increasing g , which is the opposite of the trend predicted by the numerical model. This opposing scaling in $P^* - t^*$ space implies that the interaction term utilized in the model does not reflect the observed scaling behaviour for basal fluid pressure dissipation, emphasizing the need for further investigation of the underlying mechanisms at play.

6 Discussion

The dynamic complexity of debris flows, in part, arising from their spatially and temporally evolving composition, results in significant challenges when modelling these phenomena. As such, numerical models that attempt to capture the diversity of flow behaviours observed in field-scale flows can become intractable [12] and, therefore, unsuitable for the development of effective hazard mitigation strategies. Hence, obtaining a greater understanding of the interaction between the fluid and granular phases constituting the flow is crucial to developing appropriate modelling assumptions that lead to cost-effective predictive methodologies.

In the present study, a two-phase depth averaged model was proposed to capture the essential grain-fluid

interaction processes observed during the fluid-saturated granular column collapse experiments conducted by Webb et al. [32] using elevated g -levels to reflect the grain inertia in large-scale events. The grain-fluid interaction force consists of a Darcy-drag style relation where the drag between the two phases is a function of the granular phase permeability as described by Carman's equation. The axisymmetric geometry of the experimental setup was taken advantage of by developing a system of equations that could be expressed in a conservative form using a polar coordinates system. The individual system of equations for both the fluid and granular phases can be recovered as limit cases of the two-phase system.

Numerical simulations of the experiments were undertaken with the model where its spatial and temporal discretisation were carried out using a second-order central-upwind scheme [45] and an explicit second-order Runge–Kutta method, respectively.

From initially comparing the numerical and experimental runout results of collapses consisting of a singular fluid phase, it was evident that the numerical model was significantly overestimating the initial acceleration of the fluid front. This was due to the initial configuration of the columns not adhering to the depth averaged assumption that was critical to the model's derivation. This was counteracted by employing the mass 'raining' scheme of Larrieu et al. [47] to incrementally introduce phase mass into the system, thus, eliminating the overestimation of vertical accelerations.

The ability of the tuned model was then tested by assessing how well it replicated the temporal evolution of both the granular and fluid phase fronts for a series of just-saturated granular column collapse tests where both d and g were varied. While the model could successfully replicate the acceleration, quasi-steady and retardation stages of motion expected for an unsteady mass movement, the runout distances predicted by the model overestimate those measured experimentally for every test case. The model's performance improved with decreasing d which is a key indication that this discrepancy largely emanates from the modelling assumption of a continuum granular phase. Moreover, it is important to acknowledge that this continuum approximation issue may extend to field-scale scenarios as well, as debris flows often transport boulders with diameters comparable to the flow depth. However, the model does predict a reduction in phase separation for a given d as g increases, illustrating that particle inertial effects become less dominant with increased scale.

Similarly, when comparing numerical and experimental temporal evolutions of the phase front velocity, it was hypothesised that the continuum assumption was

responsible for the model overestimating the peak phase velocities. Analysing the collapse in $u_v^* - t^*$ space also highlighted a particle-size dependent lag in the experimental data that was the result of interference from the steel column. Crucially, the initial discharge of the fluid phase was found to be heavily dependent on the permeability of the granular phase. While the influence of d on this effect increases to $g = 45.22 \text{ m s}^{-2}$, it reduces thereafter as macro-scale gravitational and viscous forces become dominant.

In order to directly compare the experimental and numerical basal fluid pressure time series, both had to undergo a reduction process to eliminate the influence of the steel column being lifted and the implementation of the mass 'raining' scheme, respectively. Comparing the datasets in $P^* - t$ space clearly showed that the model was able to replicate the strong d and g dependencies exhibited within the experimental hydrostatic pressure dissipation curves. Specifically, for a given g , the rate of pressure dissipation increases with d , while, for a given d , the rate of pressure dissipation increases with g .

Discrepancies in the magnitude of the pressure dissipation rate and the residual basal fluid pressures between the model and the experimental findings can again be reasoned to emanate from the assumption of a continuum granular phase and interference from the steel column. Additionally, analysing the trends in $P^* - t^*$ space revealed that the numerical dimensionless pressure dissipation curves decreased with increasing g , which opposes the trend observed in the experimental data. Thus, it can be determined that, while the chosen inter-phase interaction term allows the model to replicate the mechanisms governing the phase interaction at the grain-scale, it does not quite obtain the scaling behaviour observed experimentally.

Future extensions of the model would be focussed on incorporating the effects of polydispersed granular phases, meaning inertial and sub-inertial granular material, on macro-scale flow behaviour by altering the inter-phase interaction term. Webb et al. [55] explored the influence of different grain scales by conducting the same column collapse experiments as Webb et al. [32], but with a particle phase consisting primarily of inertial grains while kaolin clay particles were suspended within the fluid phase. A scale analysis of the collapse runouts found that the quantities used to characterise the phase runout were highly dependent on the degree of fines, as well as dimensionless quantities that characterised the column- and inertial grain-scales. Further testing is required to obtain basal fluid pressure evolution collapse data before the model can be extended.

Appendix A1 Model derivation

The appendix provides a detailed account of the process employed to derive the system of equations utilized in the present study from the equations presented by Meng et al. [28] who described the motion of a two-phase continuum flow that can exist in both an undersaturated and oversaturated regime. As stated by Meng et al., this unified system, which describes the motion of a two phase flow within a Cartesian coordinates system Oxz , where x and z are the directions parallel and normal to the slope inclined at an angle ζ , respectively, is as follows

$$\partial_t(h_p\phi_c) + \partial_x(h_p\phi_c\bar{u}_p) = 0, \tag{A1}$$

$$\partial_t(h_f(1 - \phi_c\mathcal{H})) + \partial_x(h_f(1 - \phi_c\mathcal{H})\bar{u}_f) = 0, \tag{A2}$$

$$\partial_t(h_p\phi_c\bar{u}_p) + \partial_x\left(\chi_p h_p \phi_c \bar{u}_p^2 + \frac{1}{2} h_p^2 \phi_c g \cos \zeta - \frac{1}{2} \gamma \phi_c (h_f \mathcal{H})^2 g \cos \zeta\right) = S_p, \tag{A3}$$

$$\partial_t(h_f(1 - \phi_c\mathcal{H})\bar{u}_f) + \partial_x\left(\chi_f h_f (1 - \phi_c\mathcal{H}) \bar{u}_f^2 + \frac{1}{2} h_f^2 g \cos \zeta\right) = S_f. \tag{A4}$$

All variables mentioned in the main text are defined as previously described, \mathcal{H} is a unifying variable that signifies the proportion of the fluid height occupied by particles, χ_v refers to phase-specific shape factors that are dependent on the prescribed phase velocity profile, and S_v are the phase-specific source terms. S_p and S_f are taken as their leading order approximations described by Meng et al. [28] with the addition of second order buoyancy effects

$$S_p = \underbrace{h_p \phi_c g \sin \zeta}_{\text{Gravity}} - \underbrace{\frac{\bar{u}_p}{|\bar{u}_p|} \left(1 - \gamma \mathcal{H} \frac{h_f}{h_p}\right) \mu_b h_p \phi_c g \cos \zeta}_{\text{Basal friction}} + \underbrace{\frac{\eta_f \phi_f^2}{\rho_p k} \min(h_f, h_p) (\bar{u}_f - \bar{u}_p)}_{\text{Darcy drag}} - \underbrace{\gamma \phi_c \mathcal{H} h_f g \cos \zeta \partial_x(h_f)}_{\text{Buoyancy}}, \tag{A5}$$

$$S_f = \underbrace{h_f(1 - \phi_c\mathcal{H})g \sin \zeta}_{\text{Gravity}} - \underbrace{C_f \bar{u}_f |\bar{u}_f|}_{\text{Chézy drag}} + \underbrace{\frac{\eta_f \phi_f^2}{\rho_f k} \min(h_f, h_p) (\bar{u}_p - \bar{u}_f)}_{\text{Darcy drag}} + \underbrace{\phi_c \mathcal{H} h_f g \cos \zeta \partial_x(h_f)}_{\text{Buoyancy}}, \tag{A6}$$

where, again, all previously seen variables are defined as they were in the main text and C_f is the Chézy drag coefficient. It should be noted that instead of using the difference in the phase streamfunction ψ_v to help define the interphase coupling term, we employ the approximations $\frac{\eta_f \phi_f^2}{\rho_p k} \min(h_f, h_p) (\bar{u}_f - \bar{u}_p)$ and $\frac{\eta_f \phi_f^2}{\rho_p k} \min(h_f, h_p) (\bar{u}_p - \bar{u}_f)$ for the particle and fluid phases, respectively. As we are looking to obtain a model which assumes that the granular phase is never oversaturated, inclusion of the min function is worthwhile, given that this may not be true for all numerical solutions.

To simplify the model, we only consider the undersaturated flow regime by assuming $\mathcal{H} = 1$ and also prescribe a plug flow velocity profile to both phases (i.e. $\chi_p = \chi_f = 1$). As our granular-fluid mixture spreads across a horizontal plane, we set ζ to 0. Additionally, we assume that fluid basal drag arising from fluid turbulence is negligible by setting $C_f = 0$. This simplification is computationally advantageous, as the fluid basal friction term can become numerically challenging when approximating \bar{u}_f as the ratio between fluid discharge and h_f [46]. By substituting equations A5 and A6 into equations A3 and A4, and using the conditions $\phi_p = \phi_c$, $\phi_f = (1 - \phi_c)$ and ϕ_c is a constant, we obtain the following system of equations

$$\partial_t(h_p) + \partial_x(h_p\bar{u}_p) = 0, \tag{A7}$$

$$\partial_t(h_f) + \partial_x(h_f\bar{u}_f) = 0, \tag{A8}$$

$$\begin{aligned} \partial_t(h_p\bar{u}_p) + \partial_x\left(h_p\bar{u}_p^2 + \frac{1}{2} h_p^2 g\right) &= \frac{\bar{u}_p}{|\bar{u}_p|} \left(1 - \gamma \frac{h_f}{h_p}\right) \mu_b h_p g \\ &+ \frac{\eta_f \phi_f^2}{\rho_p \phi_p k} \min(h_f, h_p) (\bar{u}_f - \bar{u}_p), \end{aligned} \tag{A9}$$

$$\begin{aligned} \partial_t(h_f\bar{u}_f) + \partial_x\left(h_f\bar{u}_f^2 + \frac{1}{2} h_f^2 g\right) &= \frac{\eta_f \phi_f}{\rho_f k} \min(h_f, h_p) (\bar{u}_p - \bar{u}_f). \end{aligned} \tag{A10}$$

Considering the experimental configuration, it is advantageous to transform the system of equations A7–A10 from a Cartesian to an axisymmetric reference frame. This transformation eliminates the dependence on the polar angle [56], making the results applicable to flows without lateral boundaries, such as the case of axisymmetric collapses where the flow expands over an open slope, forming a fan. Utilising polar coordinates, we can express each non-conservative flux

term K as the summation of a conservative flux term and a source term

$$\frac{1}{r} \partial_r(K(r, t)r) = \partial_r(K(r, t)) + \frac{1}{r} K(r, t), \quad (\text{A11})$$

where r is the radial spatial dimension. Then, the system of equations A7–A10 can be expressed in the following conservative form

$$\partial_t h_p + \partial_r(h_p \bar{u}_p) = -\frac{h_p \bar{u}_p}{r}, \quad (\text{A12})$$

$$\partial_t h_f + \partial_r(h_f \bar{u}_f) = -\frac{h_f \bar{u}_f}{r}, \quad (\text{A13})$$

$$\begin{aligned} \partial_t(h_p \bar{u}_p) + \partial_r\left(h_p \bar{u}_p^2 + \frac{1}{2} g h_p^2\right) \\ = -\frac{h_p \bar{u}_p^2}{r} - \mu_b \frac{\bar{u}_p}{|\bar{u}_p|} g h_p \left(1 - \gamma \frac{h_f}{h_p}\right) \\ + \frac{\eta_f \phi_f^2}{\rho_p \phi_p k} \min(h_f, h_p)(\bar{u}_f - \bar{u}_p), \end{aligned} \quad (\text{A14})$$

$$\begin{aligned} \partial_t(h_f \bar{u}_f) + \partial_r\left(h_f \bar{u}_f^2 + \frac{1}{2} g h_f^2\right) \\ = -\frac{h_f \bar{u}_f^2}{r} + \frac{\eta_f \phi_f}{\rho_f k} \min(h_f, h_p)(\bar{u}_p - \bar{u}_f). \end{aligned} \quad (\text{A15})$$

The use of a conservative approach offers several advantages. Firstly, it ensures the accurate preservation of mass and momentum conservation across phase interfaces, enabling the correct representation of jump conditions [28]. Secondly, from a numerical perspective, employing the conservative formulation proves beneficial, facilitating more efficient and accurate solutions of the system [57]. The resulting system of equations A12–A15 allows us to predict the behaviour of the system in terms of conservative quantities such as h_v and $h_v u_v$ for each phase, respectively.

Acknowledgements The authors would like to acknowledge the contributions of Sam Cook, Steve Lawton and Harry Hardy for assisting with the development and operation of the experimental apparatus.

Funding Funding provided by the EPSRC through the doctoral training grant EP/T517902/1.

Declarations

Conflict of interest The authors declare that they have no conflict of interest.

Open Access This article is licensed under a Creative Commons Attribution 4.0 International License, which permits use, sharing, adaptation, distribution and reproduction in any medium or format, as long as you give appropriate credit to the original author(s) and the source,

provide a link to the Creative Commons licence, and indicate if changes were made. The images or other third party material in this article are included in the article's Creative Commons licence, unless indicated otherwise in a credit line to the material. If material is not included in the article's Creative Commons licence and your intended use is not permitted by statutory regulation or exceeds the permitted use, you will need to obtain permission directly from the copyright holder. To view a copy of this licence, visit <http://creativecommons.org/licenses/by/4.0/>.

References

- Warnett, J., Denissenko, P., Thomas, P., Kiraci, E., Williams, M.: Scalings of axisymmetric granular column collapse. *Granular Matter* **16**(1), 115–124 (2014). <https://doi.org/10.1007/s10035-013-0469-x>
- Jakob, M., Hungr, O., Jakob, D.M.: Debris-flow hazards and related phenomena. vol. 739. Springer; (2005)
- Delannay, R., Valance, A., Mangeney, A., Roche, O., Richard, P.: Granular and particle-laden flows: from laboratory experiments to field observations. *J. Phys. D-Appl. Phys.* **50**(5), 053001 (2017). <https://doi.org/10.1088/1361-6463/50/5/053001>
- Nadim, F., Kjekstad, O., Peduzzi, P., Herold, C., Jaedicke, C.: Global landslide and avalanche hotspots. *Landslides* **3**(2), 159–173 (2006). <https://doi.org/10.1007/s10346-006-0036-1>
- Rodolfo, K.S., Lagmay, A.M.F., Eco, R.C., Herrero, T.M.L., Mendoza, J.E., Minimo, L.G., et al.: The December 2012 Mayo River debris flow triggered by Super Typhoon Bopha in Mindanao, Philippines: lessons learned and questions raised. *Nat. Hazard.* **16**(12), 2683–2695 (2016)
- Redshaw, P., Boon, D., Campbell, G., Willis, M., Mattai, J., Free, M., et al.: The 2017 Regent Landslide, Freetown Peninsula, Sierra Leone. *Q. J. Eng. Geol. Hydrogeol.* **52**(4), 435–444 (2019)
- Allen, S.K., Rastner, P., Arora, M., Huggel, C., Stoffel, M.: Lake outburst and debris flow disaster at Kedarnath, June 2013: hydrometeorological triggering and topographic predisposition. *Landslides* **13**(6), 1479–1491 (2016). <https://doi.org/10.1007/s10346-015-0584-3>
- Sati, V.P.: Glacier bursts-triggered debris flow and flash flood in Rishi and Dhaulti Ganga valleys: a study on its causes and consequences. *Nat. Hazards Res.* **2**(1), 33–40 (2022)
- Grimsley, K.J., Rathburn, S.L., Friedman, J.M., Mangano, J.F.: Debris flow occurrence and sediment persistence, upper colorado river valley. *CO. Environ. Manage.* **58**(1), 76–92 (2016). <https://doi.org/10.1007/s00267-016-0695-1>
- Oakley, N.S., Cannon, F., Munroe, R., Lancaster, J.T., Gomberg, D., Ralph, F.M.: Brief communication: Meteorological and climatological conditions associated with the 9 January 2018 post-fire debris flows in Montecito and Carpinteria, California, USA. *Nat. Hazard.* **18**(11), 3037–3043 (2018). <https://doi.org/10.5194/nhess-18-3037-2018>
- Pierson, T.C.: Distinguishing between debris flows and floods from field evidence in small watersheds. *US Geol. Surv.* 2327-6932 (2005)
- Turnbull, B., Bowman, E.T., McElwaine, J.N.: Debris flows: Experiments and modelling. *C R Phys.* **16**(1), 86–96 (2015). <https://doi.org/10.1016/j.crhy.2014.11.006>
- Iverson, R.M.: The physics of debris flows. *Rev. Geophys.* **35**(3), 245–296 (1997). <https://doi.org/10.1029/97RG00426>

14. Takahashi, T.: Debris Flow. *Annu. Rev. Fluid Mech.* **13**(1), 57–77 (1981). <https://doi.org/10.1146/annurev.fl.13.010181.000421>
15. Takebayashi, H., Fujita, M.: Numerical simulation of a debris flow on the basis of a two-dimensional continuum body model. *Geosciences*. **10**(2), 45 (2020)
16. Iverson, R.M., Denlinger, R.P.: Flow of variably fluidized granular masses across three-dimensional terrain: 1. Coulomb mixture theory. *J. Geophys. Res.: Solid Earth*. **106**(B1):537–552. (2001) <https://doi.org/10.1029/2000JB900329>
17. Berzi, D., Jenkins, J.T.: A theoretical analysis of free-surface flows of saturated granular-liquid mixtures. *J. Fluid Mech.* **608**, 393–410 (2008). <https://doi.org/10.1017/S0022112008002401>
18. Savage, S.B., Hutter, K.: The motion of a finite mass of granular material down a rough incline. *J. Fluid Mech.* **199**, 177–215 (1989). <https://doi.org/10.1017/S0022112089000340>
19. Iverson, R.M.: The debris-flow rheology myth; 2003. p. 303–314. Available from: <https://citeseerx.ist.psu.edu/viewdoc/download?doi=10.1.1.722.3486&rep=rep1&type=pdf>
20. McCoy, S.W., Kean, J.W., Coe, J.A., Staley, D.M., Waskiewicz, T.A., Tucker, G.E.: Evolution of a natural debris flow: In situ measurements of flow dynamics, video imagery, and terrestrial laser scanning. *Geology* **38**(8), 735–738 (2010). <https://doi.org/10.1130/g30928.1>
21. McArdell, B.W., Bartelt, P., Kowalski, J.: Field observations of basal forces and fluid pore pressure in a debris flow. *Geophys. Res. Lett.* **34**(7). (2007) <https://doi.org/10.1029/2006GL029183>
22. Johnson, C.G., Kokelaar, B.P., Iverson, R.M., Logan, M., LaHusen, R.G., Gray JMNT. Grain-size segregation and levee formation in geophysical mass flows. *J. Geophys. Res.: Earth Surf.* **117**(F1):n/a–n/a. (2012) <https://doi.org/10.1029/2011JF002185>
23. Pitman, E.B., Le, L.: A two-fluid model for avalanche and debris flows. *Philos. Trans.: Math., Phys. Eng. Sci.* **2005**(363), 1573–1601 (1832)
24. Iverson, R.M., George, D.L.: A depth-averaged debris-flow model that includes the effects of evolving dilatancy. I. Physical basis. *Proc. R. Soc. A: Math., Phys. Eng. Sci.* **470**(2170):20130819. (2014) <https://doi.org/10.1098/rspa.2013.0819>
25. Kowalski, J., McElwaine, J.N.: Shallow two-component gravity-driven flows with vertical variation. *J. Fluid Mech.* **714**, 434–462 (2013)
26. Gray, J.M.N.T., Kokelaar, B.P.: Large particle segregation, transport and accumulation in granular free-surface flows. *J. Fluid Mech.* **652**, 105–137 (2010). <https://doi.org/10.1017/S002211201000011X>
27. Bouchut, F., Fernández-Nieto, E.D., Koné, E.H., Mangeney, A., Narbona-Reina, G.: A two-phase solid-fluid model for dense granular flows including dilatancy effects: comparison with submarine granular collapse experiments. *EPJ Web of Conf.* **140**, 09039 (2017). <https://doi.org/10.1051/epjconf/201714009039>
28. Meng, X., Johnson, C.G., Gray, JMNT. Formation of dry granular fronts and watery tails in debris flows. *J. Fluid Mech.* **943**. (2022) <https://doi.org/10.1017/jfm.2022.400>
29. De Haas, T., Braat, L., Leuven, J.R.F.W., Lokhorst, I.R., Kleinhans, M.G.: Effects of debris flow composition on runout, depositional mechanisms, and deposit morphology in laboratory experiments. *J. Geophys. Res. Earth Surf.* **120**(9), 1949–1972 (2015). <https://doi.org/10.1002/2015jf003525>
30. Roelofs, L., Colucci, P., Haas, T.: How debris-flow composition affects bed erosion quantity and mechanisms: An experimental assessment. *Earth Surf. Proc. Land.* (2022). <https://doi.org/10.1002/esp.5369>
31. Kaitna, R., Palucis, M.C., Yohannes, B., Hill, K.M., Dietrich, W.E.: Effects of coarse grain size distribution and fine particle content on pore fluid pressure and shear behavior in experimental debris flows. *J. Geophys. Res. Earth Surf.* **121**(2), 415–441 (2016). <https://doi.org/10.1002/2015JF003725>
32. Webb, W., Heron, C., Turnbull, B.: Inertial effects in just-saturated axisymmetric column collapses. *Granular Matter* **25**(2), 40 (2023). <https://doi.org/10.1007/s10035-023-01326-x>
33. Lube, G., Huppert, H.E., Sparks, R.S.J., Hallworth, M.A.: Axisymmetric collapses of granular columns. *J. Fluid Mech.* **508**, 175–199 (2004). <https://doi.org/10.1017/S0022112004009036>
34. Lajeunesse, E., Mangeney-Castelnau, A., Vilotte, J.P.: Spreading of a granular mass on a horizontal plane. *Phys. Fluids* **16**(7), 2371–2381 (2004). <https://doi.org/10.1063/1.1736611>
35. Thompson, E.L., Huppert, H.E.: Granular column collapses: further experimental results. *J. Fluid Mech.* **575**, 177–186 (2007). <https://doi.org/10.1017/S0022112006004563>
36. Bougouin, A., Lacaze, L.: Granular collapse in a fluid: Different flow regimes for an initially dense-packing. *Phys. Rev. Fluids.* **3**(6), 064305 (2018). <https://doi.org/10.1103/PhysRevFluids.3.064305>
37. Cabrera, M., Estrada, N.: Granular column collapse: Analysis of grain-size effects. *Phys. Rev. E* **99**(1), 012905 (2019). <https://doi.org/10.1103/PhysRevE.99.012905>
38. Iverson, R.M.: Scaling and design of landslide and debris-flow experiments. *Geomorphology* **244**, 12 (2015)
39. Heller, V.: Scale effects in physical hydraulic engineering models. *J. Hydraul. Res.* **49**(3), 293–306 (2011)
40. Taylor, R.N.: *Geotechnical centrifuge technology*. New York: Blackie Academic & Professional; (1995). Available from: <https://www.taylorfrancis.com/books/e/9780203210536>
41. Pailha, M., Pouliquen, O.: A two-phase flow description of the initiation of underwater granular avalanches. *J. Fluid Mech.* **633**, 115–135 (2009). <https://doi.org/10.1017/s0022112009007460>
42. Goharzadeh, A., Khalili, A., Jørgensen, B.B.: Transition layer thickness at a fluid-porous interface. *Phys. Fluids* **17**(5), 057102 (2005). <https://doi.org/10.1063/1.1894796>
43. Ouriemi, M., Aussillous, P., Guazzelli, E.: Sediment dynamics. Part 1. Bed-load transport by laminar shearing flows. *J. Fluid Mech.* **636**, 295–319 (2009). <https://doi.org/10.1017/S0022112009007915>
44. Guérin, A., Devauchelle, O., Lajeunesse, E.: Response of a laboratory aquifer to rainfall. *J. Fluid Mech.* **759**. (2014) <https://doi.org/10.1017/jfm.2014.590>
45. Kurganov, A., Petrova, G.: A Second-Order Well-Balanced Positivity Preserving Central-Upwind Scheme for the Saint-Venant System. *Commun. Math. Sci.* **5**(1), 133–160 (2007). <https://doi.org/10.4310/CMS.2007.v5.n1.a6>
46. Chertock, A., Cui, S., Kurganov, A., Wu, T.: Well-balanced positivity preserving central-upwind scheme for the shallow water system with friction terms. *Int. J. Numer. Meth. Fluids* **78**(6), 355–383 (2015). <https://doi.org/10.1002/ld.4023>
47. Larrieu, E., Staron, L., Hinch, E.J.: Raining into shallow water as a description of the collapse of a column of grains. *J. Fluid Mech.* **554**(-1):259. (2006) <https://doi.org/10.1017/s0022112005007974>
48. Lube, G., Huppert, H.E., Sparks, R.S.J., Freundt, A.: Collapses of two-dimensional granular columns. *Phys. Rev. E.* **72**(4), (2005). <https://doi.org/10.1103/physreve.72.041301>
49. Ng, C.W.W., Choi, C.E., Koo, R., Goodwin, S., Song, D., Kwan, J.S.: Dry granular flow interaction with dual-barrier systems. *Géotechnique*. **68**(5), 386–399 (2018)
50. Leonardi, A., Cabrera, M.A., Pirulli, M.: Coriolis-induced instabilities in centrifuge modeling of granular flow. *Granular Matter* **23**(2), 52 (2021). <https://doi.org/10.1007/s10035-021-01111-8>
51. Batchelor, G.K.: *An Introduction to Fluid Dynamics*. Cambridge Mathematical Library. Cambridge: Cambridge University Press;

2000. Available from: <https://www.cambridge.org/core/books/an-introduction-to-fluid-dynamics/18AA1576B9C579CE25621E80F9266993>
52. Sarlin, W., Morize, C., Sauret, A., Gondret, P.: Collapse dynamics of dry granular columns: From free-fall to quasistatic flow. *Phys. Rev. E* **104**(6) (2021). <https://doi.org/10.1103/physreve.104.064904>
 53. Li, P., Wang, D., Niu, Z.: Unchannelized collapse of wet granular columns in the pendular state: Dynamics and morphology scaling. *Phys. Rev. Fluids* **7**(8) (2022). <https://doi.org/10.1103/physrevfluids.7.084302>
 54. Iverson, R.M.: Regulation of landslide motion by dilatancy and pore pressure feedback. *J. Geophys. Res.: Earth Surf.* **110**(F2) (2005). <https://doi.org/10.1029/2004JF000268>
 55. Webb, W., Heron, C., Turnbull, B.: Fines-controlled drainage in just-saturated, inertial column collapses. *E3S Web of Conf.* **2023**;415:01030. <https://doi.org/10.1051/e3sconf/202341501030>
 56. Alcrudo, F., Garcia-Navarro, P.: A high-resolution Godunov-type scheme in finite volumes for the 2D shallow-water equations. *Int. J. Numer. Meth. Fluids* **16**(6), 489–505 (1993). <https://doi.org/10.1002/flid.1650160604>
 57. Kurganov, A., Tadmor, E.: New High-Resolution Central Schemes for Nonlinear Conservation Laws and Convection-Diffusion Equations. *J. Comput. Phys.* **160**(1), 241–282 (2000). <https://doi.org/10.1006/jcph.2000.6459>

Publisher's Note Springer Nature remains neutral with regard to jurisdictional claims in published maps and institutional affiliations.